



# Photocatalytic Degradation of Rhodamine B via Fe-g-C<sub>3</sub>N<sub>4</sub> Activated Sulfate Radical-Based Advanced Oxidation Processes and the Synergistic Mechanism

Xinyuan Zhan<sup>1,2</sup> · Zhixiang She<sup>1,2</sup> · Zhengbo Yue<sup>1,2</sup> · Fupeng Hu<sup>1,2</sup> · Guangcheng Wang<sup>3</sup> · Shaoping Wang<sup>3</sup> · Wei Li<sup>3</sup> · Bing Liu<sup>3</sup> · Jin Wang<sup>1,2</sup>

Received: 14 November 2022 / Revised: 28 January 2023 / Accepted: 22 February 2023 / Published online: 7 February 2024

© The Author(s), under exclusive licence to Korean Institute of Chemical Engineers, Seoul, Korea 2024

## Abstract

Fe-doped g-C<sub>3</sub>N<sub>4</sub> has been proven to have the potential of visible light photocatalysis, but its catalytic activity of peroxy-monosulfate (PMS) is neglected. Herein, the complex advanced oxidation processes of Fe-g-C<sub>3</sub>N<sub>4</sub> mediated PMS and visible light photocatalysis was developed, named as Vis/Fe-g-C<sub>3</sub>N<sub>4</sub>/PMS system, whose effects and synergistic mechanism for decomposing Rhodamine B (RhB) was evaluated. The coupling of sulfate radicals and photocatalysis for RhB degradation showed that the synergistic efficiency ( $\eta_{\text{Syn}}$ ) and factor ( $S_c$ ) were 20.1% and 4.82, respectively, with a degradation efficiency of 99.8%. Iron species dispersed on g-C<sub>3</sub>N<sub>4</sub> provided active sites for PMS activation to generate sulfate radicals, simultaneously reduced the forbidden band, and separated the photo-generated charges of g-C<sub>3</sub>N<sub>4</sub>.  $h^+$ ,  $\text{SO}_4^{\cdot-}$  and  $^1\text{O}_2$  were the main active species, and the increase of  $^1\text{O}_2$  was the cause of the synergistic effect. The possible degradation path of RhB by this coupling system was proposed. Our findings prove that Vis/Fe-g-C<sub>3</sub>N<sub>4</sub>/PMS system has a great potential to decompose dye wastewater, and also to be an environmental remediation perspective.

**Keywords** Fe-g-C<sub>3</sub>N<sub>4</sub> · Photocatalysis · Advanced oxidation processes · Sulfate radical · Rhodamine B · Synergistic mechanism

## Introduction

In spite of contributing to the progress of human civilization, urbanization, and industrialization results in massive industrial wastewater discharge. Industrial effluents from organic dyestuff use in industries like papermaking, textile printing/dyeing, and cosmetic without control posed a threat to human health and the ecosystem due to their high toxicity (mutagenic, xenobiotic, and carcinogenic) and color [20, 23, 29, 38]. In which, textile industry as the largest discharge

resource of dye wastewater had been estimated around 0.2 million tonnes of dye/year swept into it [29]. Therefore, it is an urgent issue for treating dye wastewater, which become the research hot-point in the wastewater treatment field [4].

To date, the approaches to disposing of dye wastewater include physiochemical (adsorption, flocculation, and membrane separation) [3, 12, 19, 36, 51], abiotic processes [53, 54] and chemical methods (electrochemical oxidation and advanced oxidation processes) [1, 2, 12, 16, 18, 37]. Compared with traditional methods, advanced oxidation processes (AOPs) have the advantage of being environment-friendly and high-efficiency, in which the photocatalytic degradation process attracts more attention for persistent organic pollutant decomposition due to completely devastating pollutants, safe and eco-friendly reactants [6, 29, 41, 42].

Rhodamine B (RhB), as the best-known representative of water-soluble dye, had been photocatalytic decomposed at 88.2% removal by heterojunction photocatalyst of In<sub>2</sub>S<sub>3</sub>/Bi<sub>2</sub>MoO<sub>6</sub> [9]. Photocatalytic degradation has a high-efficiency degradation for RhB, but metal-based photocatalyst needs high cost and pose the risk of leaching toxicity [9, 43].

✉ Jin Wang  
sophiawj@hfut.edu.cn

<sup>1</sup> School of Resources and Environmental Engineering, Hefei University of Technology, Hefei 230009, Anhui, China

<sup>2</sup> Key Laboratory of Nanominerals and Pollution Control of Anhui Higher Education Institutes, Hefei University of Technology, Hefei 230009, Anhui, China

<sup>3</sup> Nanshan Mining Company Ltd, Anhui Maanshan Iron and Steel Mining Resources Group, Maanshan 243000, Anhui, China

In contrast, a small band gap and non-metal photocatalyst have been found and applied for photocatalytic decomposing RhB, which is graphitic phase carbon nitride (g-C<sub>3</sub>N<sub>4</sub>) [50]. However, the enhanced photocatalytic mechanism of g-C<sub>3</sub>N<sub>4</sub> was not be further explored, in special for the RhB degradation mechanism. Note that g-C<sub>3</sub>N<sub>4</sub> is a new photocatalyst and has the advantages of energy band, light absorption, and physiochemical properties easily adjusted, resulting in enormous attention on the photocatalytic field [8]. Therefore, the low-cost and narrow band gap of g-C<sub>3</sub>N<sub>4</sub> plays a virtual role in the field of AOPs treating dye wastewater.

The preparation methods of g-C<sub>3</sub>N<sub>4</sub> include the physical method (ion implantation, laser beam sputtering, and reactive sputtering) and the chemical method (solvothermal method, electrochemical deposition, thermal polymerization, and solid-state reaction methods) [24]. Among these, thermal pyrolysis become the mainstream for preparing g-C<sub>3</sub>N<sub>4</sub> due to its simple practice. However, volume phase g-C<sub>3</sub>N<sub>4</sub> has some disadvantages such as small surface area, low visible light utilization rate, and difficult separation of carriers generated from light irradiation. Therefore, g-C<sub>3</sub>N<sub>4</sub> needs to be modified, including template optimal of structure [21], elements doping or condensation of energy band structure [8], precious metals participating, and semiconductor compound [30]. The doping method was widely used to adjust the visual, manganite, and performances of semiconductors. Fe<sup>3+</sup> doping in g-C<sub>3</sub>N<sub>4</sub> enhanced its absorption capacity of visible light and cut down the compound rate of carriers [34].

The Fe doping g-C<sub>3</sub>N<sub>4</sub> was synthesized for photocatalytic degradation of RhB, while the catalytic enhanced mechanism and other catalytic performance of Fe doping g-C<sub>3</sub>N<sub>4</sub> were neglected [50]. For instance, Fe<sup>2+</sup> can activate persulfate to generate SO<sub>4</sub><sup>•-</sup>, and g-C<sub>3</sub>N<sub>4</sub> has the same effect [25, 49]. Besides, sulfate radical (SR, SO<sub>4</sub><sup>•-</sup>) has higher oxidation–reduction potential and wider pH adaptability compared with the hydroxyl radical (•OH) on tackling RhB [26, 31]. Therefore, Fe doping g-C<sub>3</sub>N<sub>4</sub> collaborated with peroxymonosulfate (PMS) and photocatalysis (Vis/Fe-g-C<sub>3</sub>N<sub>4</sub>/PMS) was used to decompose RhB for sufficiently exploring the potential of Fe doping g-C<sub>3</sub>N<sub>4</sub>. The decomposition and synergistic mechanism were revealed and provided by Ultraviolet–Visible diffuse reflectance spectrometry, Fourier transform infrared spectroscopy, X-ray photoelectron spectrometry, radical quenching experiment, and liquid chromatography-mass spectrometry. The synergistic and innovative method of combining Fe-g-C<sub>3</sub>N<sub>4</sub>, PMS, and photocatalysis can become a potential approach to decomposing dye wastewater.

## Materials and Methods

### Experimental Chemicals

Rhodamine B (C<sub>28</sub>H<sub>31</sub>ClN<sub>2</sub>O<sub>3</sub>), ferric sulfate (Fe<sub>2</sub>(SO<sub>4</sub>)<sub>3</sub>), cyanuramide (C<sub>3</sub>H<sub>6</sub>N<sub>6</sub>), potassium mono-persulfate triple salt (KHSO<sub>5</sub>·0.5KHSO<sub>4</sub>·0.5K<sub>2</sub>SO<sub>4</sub>), and free radical scavengers like ethylenediaminetetraacetic acid disodium (EDTA-2Na), tert-butanol ((CH<sub>3</sub>)<sub>3</sub>COH), ethanol (C<sub>2</sub>H<sub>5</sub>OH, EtOH), sodium azide (NaN<sub>3</sub>) and 1,4-benzoquinone (BQ) were purchased from Sinopharm Chemical Reagent Co., Ltd. (Peking, China) of analytical pure. All solutions were prepared with distilled water (18.25 MΩ cm<sup>-1</sup>).

### Preparation and Characterization of Catalyst

The preparation method of g-C<sub>3</sub>N<sub>4</sub> was briefly described as follows [17]: 20 g cyanuramide was weighted and put in an alumina pot, which was sintered at 530 °C for 2 h in the semi-closed system, and then the resulting products were cooled to ambient temperature (30 °C) and labeled for g-C<sub>3</sub>N<sub>4</sub> (slight yellow). The Fe-g-C<sub>3</sub>N<sub>4</sub> preparation was based on the above method. The sintered precursor was attained by dissolving cyanuramide (30 g) in distilled water (150 ml), adding Fe<sub>2</sub>(SO<sub>4</sub>)<sub>3</sub> (0.12, 0.3, 0.6, and 0.9 g), evaporating at 100 °C and drying at 80 °C. In the end, the sintered products were labelled XFe-g-C<sub>3</sub>N<sub>4</sub>, in which X was the quality proportion of Fe<sub>2</sub>(SO<sub>4</sub>)<sub>3</sub> to cyanuramide.

The mineral phase of catalysts was determined by X-ray diffraction (XRD; Bruker D8, Germany) with CuKα radiation in the 2θ range from 10° to 80° at a scanning rate of 0.2°/s. Microstructure of catalysts was assessed by transmission electron microscope (TEM; JEOL JEM-2100, Japan) with copper web. Molecule vibration spectroscopy of catalysts was measured between wave numbers 4000 and 400 cm<sup>-1</sup> by use of Fourier transform infrared spectroscopy (FTIR; Bruker Vector 22, Germany) with KBr pellets. UV–Visible diffuse reflectance spectrometry (DRS; Shimadzu UV-2450, Japan) was used to determine photo-properties of samples with scanning wavelength between 200 and 800 nm referring to BaSO<sub>4</sub>, and the absorption spectra were attained by Kubelka–Munk function transformation. X-ray photoelectron spectrometry (XPS; Thermofisher VG Multi-lab2000, America) analysis was conducted with a spectrometer using monochromatic Al K-alpha radiation (1486.6 eV). A specific surface area analyzer (Quantachrome NOVA 3000e, America) was used to determine the surface area of catalysts by N<sub>2</sub> adsorption/desorption curves with the calculation of Brunauer–Emmett–Teller.

## Catalyst and AOPs Experiment

The catalytic experiment was performed in a photocatalytic apparatus which is shown in Fig. S1. The visible light was from a xenon lamp which was filtrated by a UV filter, with a power of 500 W (80 V and 4 A). The photocatalytic experiment was conducted and described briefly as follows: 0.04 g (Fe-g-C<sub>3</sub>N<sub>4</sub>) catalyst and 100.0 mL RhB (10 mg/L) were settled in sandwich beaker and the mixture was pre-stirred in homogenous with no-light irradiation; then the photocatalytic experiment was running with visible light irradiation, and sampling was carried out each time with the interval of 15 min; each sampler was 10 mL and centrifuged at 4000 r/min for 10 min; in the end, RhB of supernatant was determined by UV-Vis spectrophotometry at 553 nm. SR-AOPs experiment was conducted in the same setup. Constant Fe-g-C<sub>3</sub>N<sub>4</sub> was added and stirred for 60 min, then PMS was introduced for reacting 75 min under dark conditions. During the SR-AOPs experiment, each 10 ml sampler was taken with the constant interval time, and 5 mL methanol quencher was added simultaneously. The synergistic experiment of AOPs-photocatalysis (SR-AOPs/Photocatalyst) was carried out in the above procedure but with visible light irradiation. The degradation efficiency of RhB and TOC were calculated by Eqs. (1) and (2):

$$\eta_D = \frac{C_0 - C_t}{C_0} \times 100\%, \quad (1)$$

$$\eta_T = \frac{\text{TOC}_0 - \text{TOC}_t}{\text{TOC}_0} \times 100\%, \quad (2)$$

where  $\eta_D$  is the degradation efficiency of RhB,  $C_0$  and  $C_t$  (mg/L) are the initial concentration and current concentration at reacting time ( $t$ ) of RhB;  $\eta_T$  is the removal efficiency of TOC,  $\text{TOC}_0$  and  $\text{TOC}_t$  (mg/L) are the initial concentration and current concentration at sampling time ( $t$ ) of TOC.

The stability experiment of Fe-g-C<sub>3</sub>N<sub>4</sub> was briefly described as follows: used catalyst was recovered by centrifuging, filtering, washing, and drying, and then it was used in SR-AOPs/Photocatalysis system. This cycle was replicated for 5 times, and the performances of the catalyst for using 5 times were characterized by XRD, FTIR, XPS, and UV-Vis.

## RhB Degradation Mechanism

The degradation path of RhB in the Vis/Fe-g-C<sub>3</sub>N<sub>4</sub>/PMS system was determined by UV-Vis spectra and combined with high-performance liquid chromatography-mass spectrometry (HPLC-MS; Agilent, America). The free radical identification was determined by free radical quenching

experiments. The running conditions of HPLC-MS were described as follows: type of chromatographic column was Agilent® TC-C18 (4.6 mm × 150 mm); sample volume was 10 μL with the rate of 0.8 mL/min; carrier was in the mixture of methanol to water at 60/40 in volume; electron spray ionization (ESI) resource was positive mode for MS.

## Results and Discussion

### Catalyst

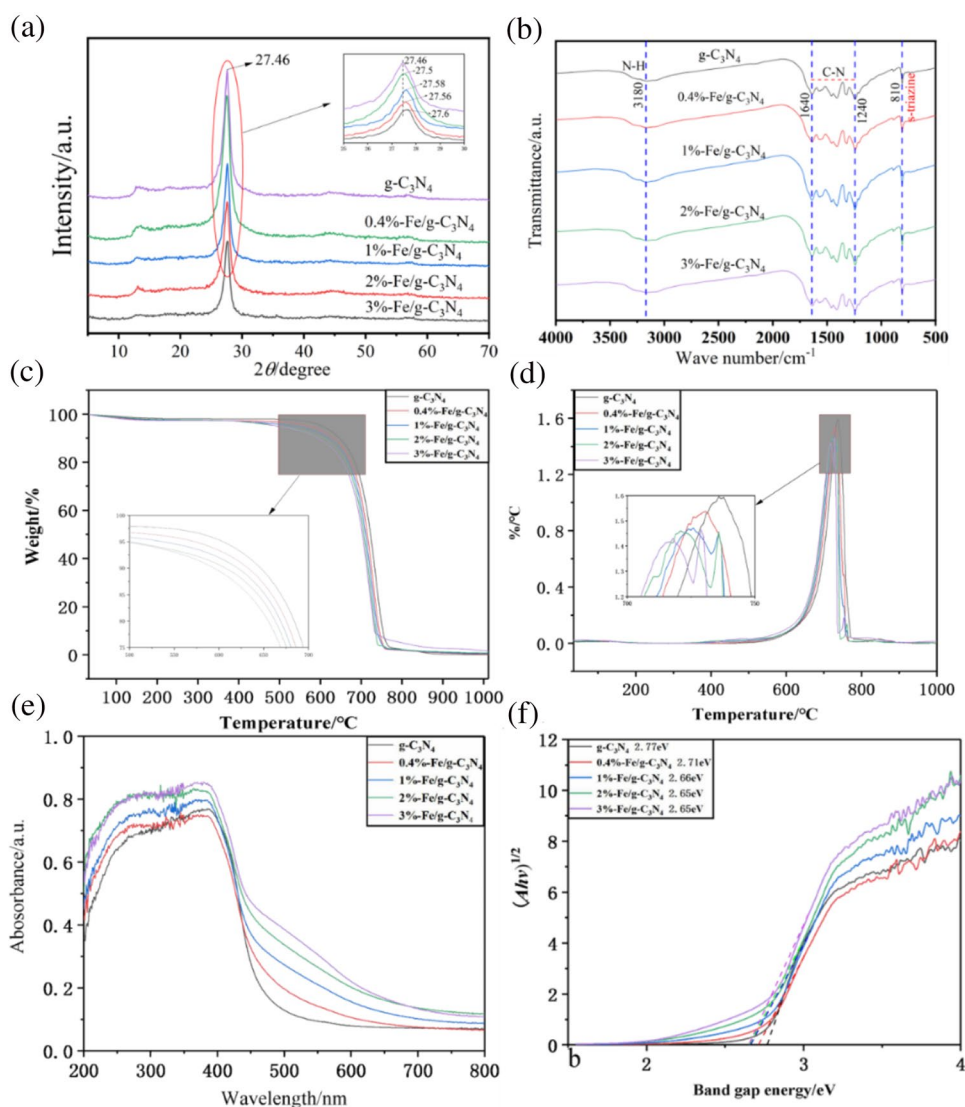
#### Characterization of Catalyst with Various Fe Contents

The physical and chemical properties are shown in Fig. 1. From XRD graphics of g-C<sub>3</sub>N<sub>4</sub> and XFe-g-C<sub>3</sub>N<sub>4</sub> (Fig. 1a), the characteristic peak at 27.5° was ascribed for inter-layer stacking of conjugated aromatics, corresponding to the (002) crystal plane of g-C<sub>3</sub>N<sub>4</sub> [13]. The weak diffraction peak of 13.5° was ascribed to in-plane stacking of a graphite-like layer (accumulation of N pores in a polymer with tri-s-triazine units), indicating melon-like materials (JCPMS87-1526) formation [7, 10]. The XRD peaks of g-C<sub>3</sub>N<sub>4</sub> and XFe-g-C<sub>3</sub>N<sub>4</sub> had no obvious difference. However, the increase of Fe content caused the characteristic peak at 27.5° shift to the large angle, which can be explained by that Fe introduction enhanced the Van der Waals forces of g-C<sub>3</sub>N<sub>4</sub> [11]. The decrease of (002) peak density caused by Fe addition indicates that Fe and g-C<sub>3</sub>N<sub>4</sub> happened interaction and Fe inhibited the polymerization and condensation of g-C<sub>3</sub>N<sub>4</sub>. However, the XRD of XFe-g-C<sub>3</sub>N<sub>4</sub> does not the diffraction peak of Fe-bearing compounds like iron oxides, iron nitrides, and iron carbides, which reveals that Fe was in the form of Fe-N coordination bond in XFe-g-C<sub>3</sub>N<sub>4</sub> [47].

The FTIR pictures of g-C<sub>3</sub>N<sub>4</sub> and XFe-g-C<sub>3</sub>N<sub>4</sub> are shown in Fig. 1b. The vibration peaks of XFe-g-C<sub>3</sub>N<sub>4</sub> were 810 cm<sup>-1</sup>, 1240–1640 cm<sup>-1</sup> and 3000–3200 cm<sup>-1</sup>, which were ascribed to bending vibration of triazine cyclic compound, vibration of C-N heterocyclic compound and stretching vibration of N-H, respectively [47]. The existence of N-H indicates that the product obtained by thermal polycondensation of melamine was incomplete polycondensation, and there were uncondensed amino groups at the edge of its layered structure. The differences among XFe-g-C<sub>3</sub>N<sub>4</sub> catalysts were not obvious, which means that the bonding structure of g-C<sub>3</sub>N<sub>4</sub> was not changed by Fe addition [14].

To reveal the thermal stability of synthetic XFe-g-C<sub>3</sub>N<sub>4</sub>s, the TG-DTA test of catalysts was performed and shown in Fig. 1c, d. The weight loss at 160 °C was due to the evaporation of water. Note that the weight loss of XFe-g-C<sub>3</sub>N<sub>4</sub> between 200 and 500 °C was not obvious, demonstrating good thermal stability. When the catalysts were heated to 600 °C, the weight loss was below 10%. However, the

**Fig. 1** Characterization of catalysts: **a** XRD; **b** FT-IR; **c** TG curves, **d** DTA curves, **e** UV–Vis diffuse reflection and **f** energy bandgap spectra



largest weight loss and exothermic peak (Fig. 1d) happened at 700–750 °C, which was attributed to the decomposition of  $C_3N_4$  and the decomposers were combusted rapidly to produce  $N_2$ , cyanide, and  $CO_2$  [30]. The weight loss between 700 and 750 °C was positive proportional to Fe content (Fig. 1c), indicating Fe addition reduced the thermal stability of catalysts. The Fe content of synthetic Fe- $g-C_3N_4$  was calculated by ultima weight at DTG and were 0%, 0.16%, 0.45%, 0.79%, and 1.20% (theoretical values were 0%, 0.16%, 0.4%, 0.8%, and 1.2%).

Figure 1e, f shows the response absorption of visible light of XFe- $g-C_3N_4$ s and their calculation for band gap. The diffuse reflection spectrum of  $g-C_3N_4$  was the representative semiconductor absorption (Fig. 1e) due to carrier shifting from the valence band (N 2p orbit) to the conduction band (C 2p orbit) [55]. The absorption edge of  $g-C_3N_4$  happened around 460 nm, but Fe addition made the absorption edge red-shift and increased their absorption

density. According to the semiconductor bandgap derivation formula, a plot of  $(Ah\nu)^{1/2}$  versus  $h\nu$  was shown in Fig. 1f. Forbidden bandwidth ( $E_g$ ) can be obtained from point tangent and X axis intersection point in Fig. 1f. The forbidden bandwidth of  $g-C_3N_4$  was 2.77 eV, and the Fe addition reduced the bandgap energy. That means negative correction of conduction band energy and positive correction of valence band energy happened, in favor of the catalyst absorbing more lights. Therefore, Fe introduction enhanced the absorption capacity of light compared with pure  $g-C_3N_4$ , indicating a stronger capacity for photocatalyst activity. But, when the Fe addition was above 1%, the decreased proportion of forbidden bandwidth was not obvious. Therefore, comprehensive consideration of thermal stability (Fig. 1c) and light absorption, 1% Fe addition was selected to be further focused on the microstructure and XPS.

## XPS and Microstructure of g-C<sub>3</sub>N<sub>4</sub> and 1%Fe-g-C<sub>3</sub>N<sub>4</sub>

The XPS and VB XPS spectra of g-C<sub>3</sub>N<sub>4</sub> and 1% Fe-g-C<sub>3</sub>N<sub>4</sub> were determined, as shown in Fig. S2 and Fig. 2. The C 1s XPS spectra in g-C<sub>3</sub>N<sub>4</sub> at 286.0 eV (Fig. 2a) was considered as sp<sup>3</sup> hybridized carbon atom in C-(N)<sub>3</sub>, and the peak at 287.9 eV was ascribed to carbon atom sp<sup>2</sup> hybrid in N-C=N backbone [56]. The N 1s spectra of g-C<sub>3</sub>N<sub>4</sub> in Fig. 2b was deconvoluted into four peaks, at 398.5, 399.0 and 404.7 eV, corresponding to sp<sup>2</sup> hybrid of C-N=C (pyridinic), N linking ring structure in N-(C)<sub>3</sub> or N layer structure in (C)<sub>2</sub>-N-H (pyrrolic), and graphitic N specie, respectively [13, 56]. However, the C 1s and N 1s spectra of 1%Fe-g-C<sub>3</sub>N<sub>4</sub> showed a higher binding energy about peak position compared with g-C<sub>3</sub>N<sub>4</sub>. This can be explained by that the Fe-N coordinate bond was formed, which means that electron cloud density around N and C decreased and the atomic nucleus had a strong capture capacity for extra-nuclear electronics. The obvious enhancement of N 1s at 398.5 eV reveals that Fe promoted the formation of C-N=C (pyridine). Note that N in pyridine was attributed to the interaction of the N-C matrix, and it was considered to be a bridge connecting carbon nitrogen polymers and carbon fragments [46]. From Fig. 2c, the Fe xp<sub>3/2</sub> spectrum was deconvoluted into three peaks at 710.1, 711.5, and 714.5 eV, corresponding to Fe<sup>2+</sup> (35.1%), Fe<sup>3+</sup> (31.1%), and satellite peaks of Fe<sup>2+</sup> and Fe<sup>3+</sup> (33.8%), respectively [48]. This generation of Fe<sup>2+</sup> might be contributed to the reaction of Fe<sup>3+</sup> with cyanuramide during sintering. In addition, the binding energy of Fe 2p<sub>1/2</sub> was concentrated on 724.3 eV, belonging

to Fe<sup>3+</sup> [33]. The VB XPS of g-C<sub>3</sub>N<sub>4</sub> and 1% Fe/g-C<sub>3</sub>N<sub>4</sub> (Fig. 2d) shows that Fe addition changed the binding energy and shifted 0.1 eV, which was consistent with the result of UV-Vis. Therefore, the structure of g-C<sub>3</sub>N<sub>4</sub> and 1% Fe-g-C<sub>3</sub>N<sub>4</sub> is further shown in Fig. 3, as determined by TEM. Edge rolled sheet structure with light color existed in g-C<sub>3</sub>N<sub>4</sub>, which means that g-C<sub>3</sub>N<sub>4</sub> had an obvious overlapping layered structure and several micrometers size, consistent with other reports [47]. Massive deposits were not found in 1%Fe-g-C<sub>3</sub>N<sub>4</sub>, indicating that Fe existed in the form of ions (Fe-N coordination bond) rather than iron or its oxides [14, 22]. Therefore, the molecule of 1%Fe-g-C<sub>3</sub>N<sub>4</sub> can be expressed in Fig. S3.

## Degradation of RhB

The adsorption equilibrium of the catalyst for RhB reached 60 min under dark conditions, then they were applied for the next experiment, as well as for PMS, which is shown in . Furthermore, the degradation kinetic curve of RhB under various reacted conditions is shown in Fig. 4. PMS addition increased the catalytic degradation efficiency of RhB (Fig. 4a), which is consistent with other report [44]. The increase of Fe content in Fe-g-C<sub>3</sub>N<sub>4</sub> boosted the degradation efficiency of RhB combined with PMS, but when iron doping further increased, the degradation efficiency decreased in return. The optimal content of Fe was 1%, which can be reflected by its microstructure, band energy structure, absorption capacity of visible light, and photogenerated carrier separation efficiency (consistent

**Fig. 2** XPS spectra of g-C<sub>3</sub>N<sub>4</sub> and 1%Fe-g-C<sub>3</sub>N<sub>4</sub> samples in the region of C 1s (a), N 1s (b), Fe 2p (c), and valence band (VB) XPS spectra of photocatalysts (d)

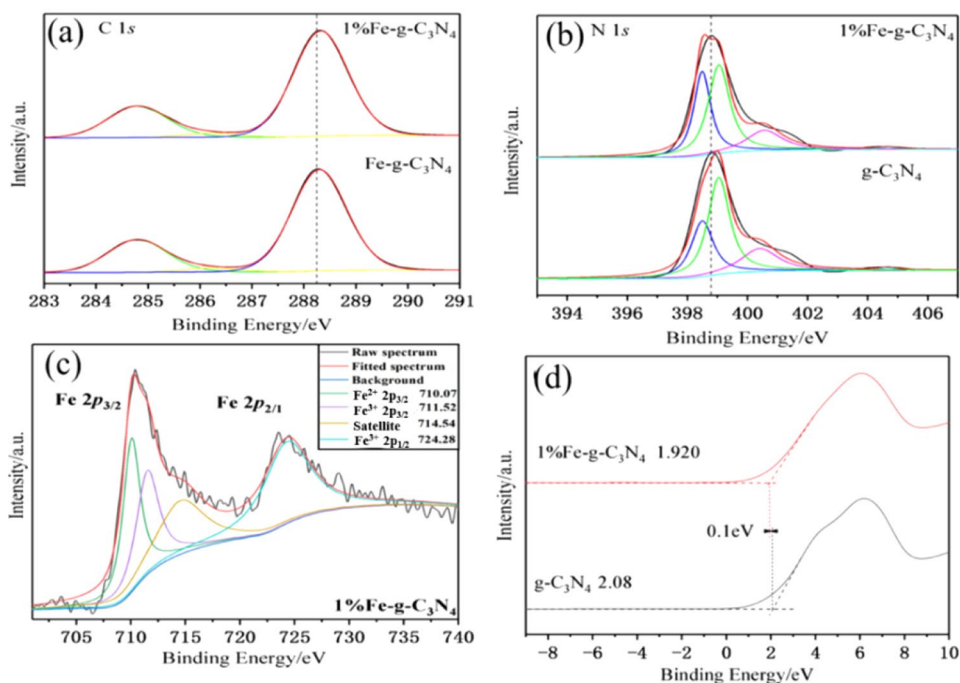
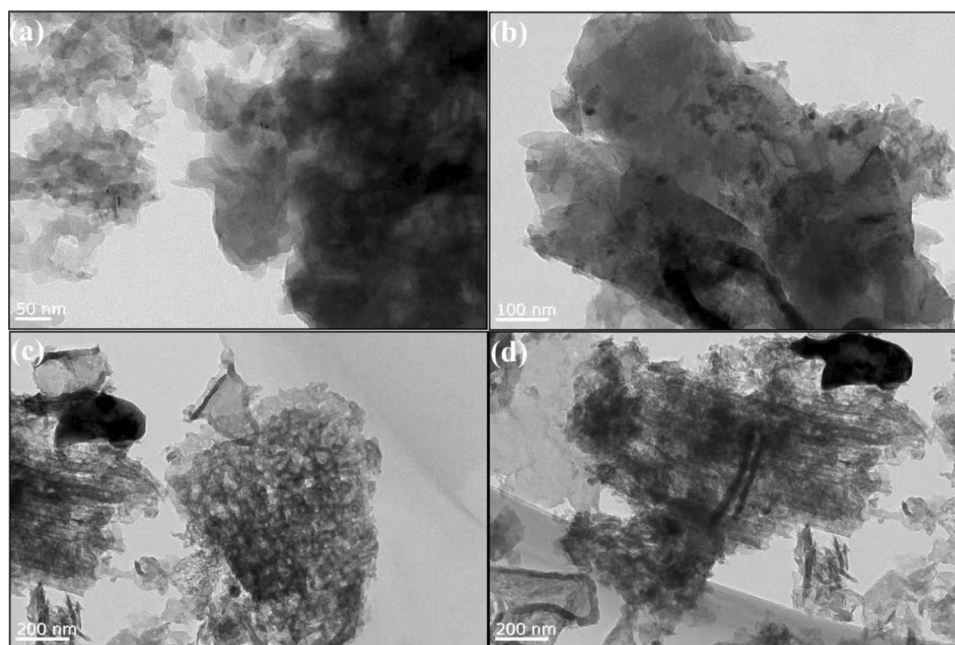


**Fig. 3** TEM images of g-C<sub>3</sub>N<sub>4</sub> (a, b) and Fe/g-C<sub>3</sub>N<sub>4</sub> photocatalysts (c, d)



with "Catalyst"). The reaction kinetics of RhB degradation by g-C<sub>3</sub>N<sub>4</sub> and Fe-g-C<sub>3</sub>N<sub>4</sub> belonged to pseudo-first-order model (Fig. 4b,  $R^2 > 0.9$ ), and the rate constants were attained from  $-\ln(C/C_0)$  versus  $t$ . The rate constant of g-C<sub>3</sub>N<sub>4</sub>, 0.4%Fe-g-C<sub>3</sub>N<sub>4</sub>, 1%Fe-g-C<sub>3</sub>N<sub>4</sub>, 2%Fe-g-C<sub>3</sub>N<sub>4</sub> and 3%Fe-g-C<sub>3</sub>N<sub>4</sub> was 0.022 min<sup>-1</sup>, 0.042 min<sup>-1</sup>, 0.086 min<sup>-1</sup>, 0.077 min<sup>-1</sup> and 0.066 min<sup>-1</sup>, respectively. The rate constant of 1%Fe-g-C<sub>3</sub>N<sub>4</sub> was the highest, 3.91 times that of pure g-C<sub>3</sub>N<sub>4</sub>. The degradation and first-order kinetic curves of RhB by different reaction systems were shown in Fig. 4c, d. The degradation ratio in Vis/Fe-g-C<sub>3</sub>N<sub>4</sub>/PMS was higher than in Vis/Fe-g-C<sub>3</sub>N<sub>4</sub> and Dark/Fe-g-C<sub>3</sub>N<sub>4</sub>/PMS. To find the effect of AOPs and photocatalysis, the synergistic efficiency ( $\eta_{\text{Syn}}$ , %) and factor ( $S_c$ ) were calculated by Eqs. (3) and (4), which are shown in Table S1.

$$\eta_{\text{Syn}} = \frac{D_{\text{SR-AOPs/Photocatalysis}} - (D_{\text{SR-AOPs}} + D_{\text{Photocatalysis}})}{D_{\text{SR-AOPs}} + D_{\text{Photocatalysis}}} \times 100\%, \quad (3)$$

$$S_c = \frac{k_{\text{SR-AOPs/Photocatalysis}}}{k_{\text{SR-AOPs}} + k_{\text{Photocatalysis}}}, \quad (4)$$

where  $D_{\text{SR-AOPs}}$  is the degradation efficiency of RhB in SR-AOPs system (%);  $D_{\text{Photocatalysis}}$  is the degradation efficiency of RhB in photocatalytic system (%);  $D_{\text{SR-AOPs/Photocatalysis}}$  is the degradation efficiency of RhB in Vis/Fe-g-C<sub>3</sub>N<sub>4</sub>/PMS system (%);  $k_{\text{SR-AOPs}}$  is the apparent rate constant of RhB degradation in SR-AOPs system (min<sup>-1</sup>);  $k_{\text{Photocatalysis}}$  is the apparent rate constant of RhB degradation in photocatalytic system (min<sup>-1</sup>);  $k_{\text{SR-AOPs/Photocatalysis}}$  is the apparent rate

constant of RhB degradation in Vis/Fe-g-C<sub>3</sub>N<sub>4</sub>/PMS system (min<sup>-1</sup>).

The synergistic efficiency ( $\eta_{\text{Syn}}$ ) and factor ( $S_c$ ) of Vis/Fe-g-C<sub>3</sub>N<sub>4</sub>/PMS were 20.1% and 4.82, which means that the compound effect of SR-AOPs and photocatalysis had increased by 20.1% compared with their linear stretching, and the synergistic action was larger. To infer the cause of the synergistic effect, the adsorption capacity and zeta potential of g-C<sub>3</sub>N<sub>4</sub> and XFe-g-C<sub>3</sub>N<sub>4</sub> were determined under the dark condition for 1 h, and shown in Fig. S4. Fe addition had a negative effect on adsorption of RhB, which can be explained by the surface charge. The zeta potential of Fe-g-C<sub>3</sub>N<sub>4</sub> was obviously higher than g-C<sub>3</sub>N<sub>4</sub>, thus the adsorption capacity of Fe-g-C<sub>3</sub>N<sub>4</sub> to positive RhB was lower than g-C<sub>3</sub>N<sub>4</sub>. That means the synergistic effect can exclude the absorption capacity and focus on the electron transformation.

## The Degradation Mechanism of RhB in Vis/Fe-g-C<sub>3</sub>N<sub>4</sub>/PMS System

### RhB Degradation Process Identification

Intermediates and degradation of RhB in Vis/Fe-g-C<sub>3</sub>N<sub>4</sub>/PMS system are shown in Fig. 5. The conditions of 0.4 g/L 1% Fe-g-C<sub>3</sub>N<sub>4</sub>, 0.4 g/L PMS and 10 mg/L RhB were selected for SR-AOPs /Photocatalysis and samplers attained with constant interval times were scanned by UV-Vis full-spectrum, which is shown in Fig. 5a. The most density of absorption peak for RhB was focused on 553 nm, and four weak peaks

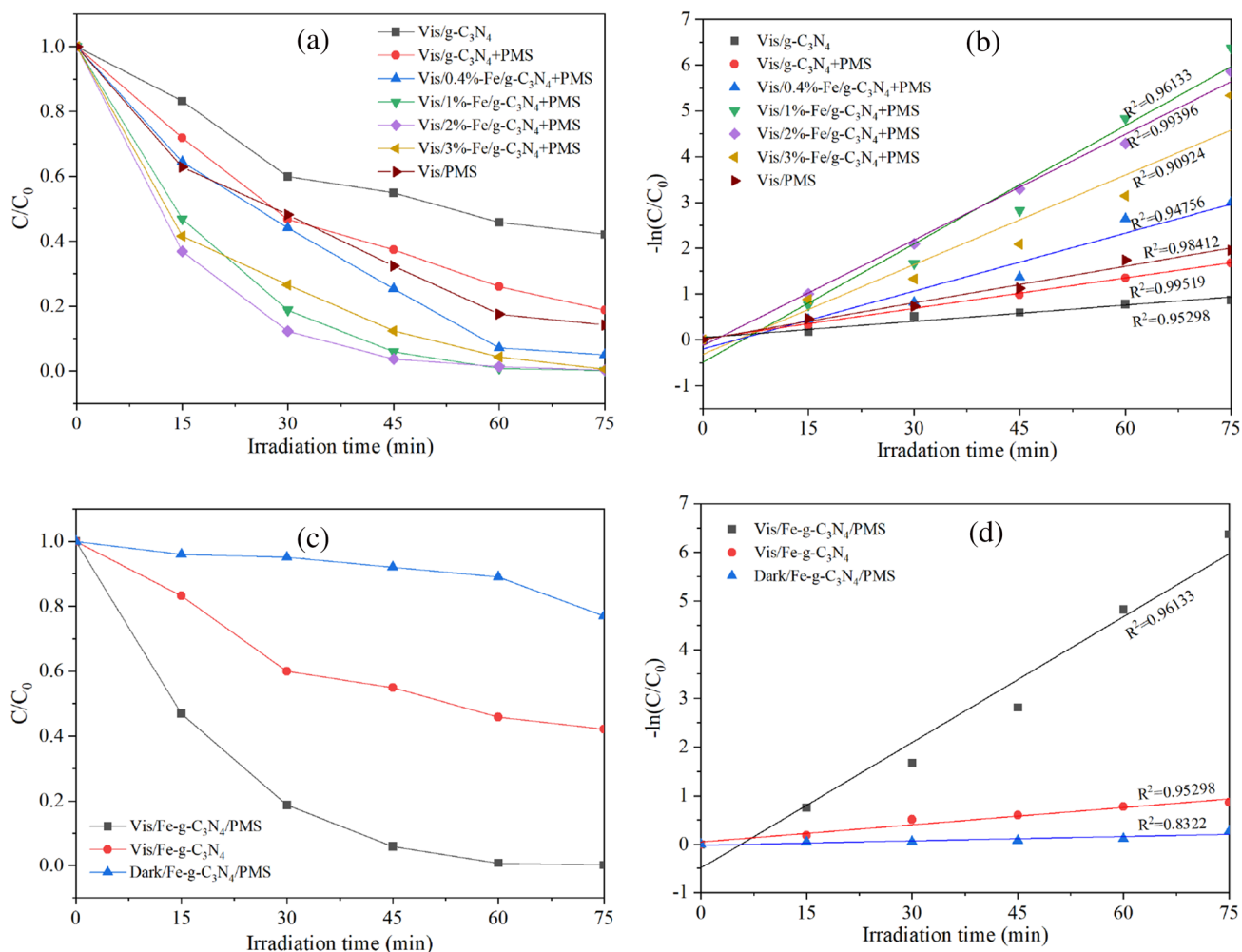


**Fig. 4** Degradation curves of RhB under various reacted conditions: **a** degradation kinetic curves of RhB; **b** first-order kinetic fitting under visible light irradiation; **c** different reaction systems and its first-order kinetic fitting (**d**)

existed in the UV wave range. These four peaks of RhB weakened after it was adsorbed for 60 min under dark conditions, which indicates fewer catalysis happening. The maximum absorption peak at 553 nm and other peaks weakened gradually with photocatalysis running, which means that phenylamino and carbonyl groups in chromogenic groups of RhB were devastated by sulfate radical oxidation. The density of the characteristic peak decreased while the position blue-shifted slightly due to the intermediates of *N*-position deethylation. Therefore, *N*-position deethylation and conjugate structure destruction of RhB happened simultaneously in the Vis/Fe-g-C<sub>3</sub>N<sub>4</sub>/PMS system, which was also found in heterogeneous AOPs catalytic degradation of RhB by Fe<sub>2</sub>(MoO<sub>4</sub>)<sub>3</sub> [28]. Sampling the degradation products of reacting 0, 15, 30, 45, 60, and 75 min was further determined by high-performance liquid chromatography-ion trap-time of flight mass spectrometer (UPLC-MS), and shown in Fig. 5b. In the absence of light irradiation, chromatography peak A

existed in RhB, while peak A decreased and was decomposed about 91% for 75 min with vis-light irradiation. Five kinds of deethylation intermediate in liquid samplers were determined in the positive ion mode. Ion peaks of these intermediates decreased orderly with 28 quality units (from A to F), consistent with deethylation of RhB and shift of absorption peak in UV-Vis Spectra (Fig. 5a). The peaks range from A to F were ascribed to RhB, *N*, *N*-diethyl-*N'*-ethyl rhodamine (DER), *N*-ethyl-*N'*-ethyl rhodamine (EER), *N*, *N*-diethyl rhodamine (DR), *N*-ethyl rhodamine (ER) and rhodamine (R), respectively. In negative ion mode, benzoic acid, phthalate, and *p*-hydroxybenzoic acid were determined, consistent with relative researches [12, 27, 31]. The intermediates of RhB degradation were further decomposed into various small molecule acids, including benzoic acid, glutaric acid, succinic acid, malonic acid, ethylenediamine acid, acetic acid, and formic acid. Total organic carbon (TOC) can characterize the mineralized degree of organics. The TOC

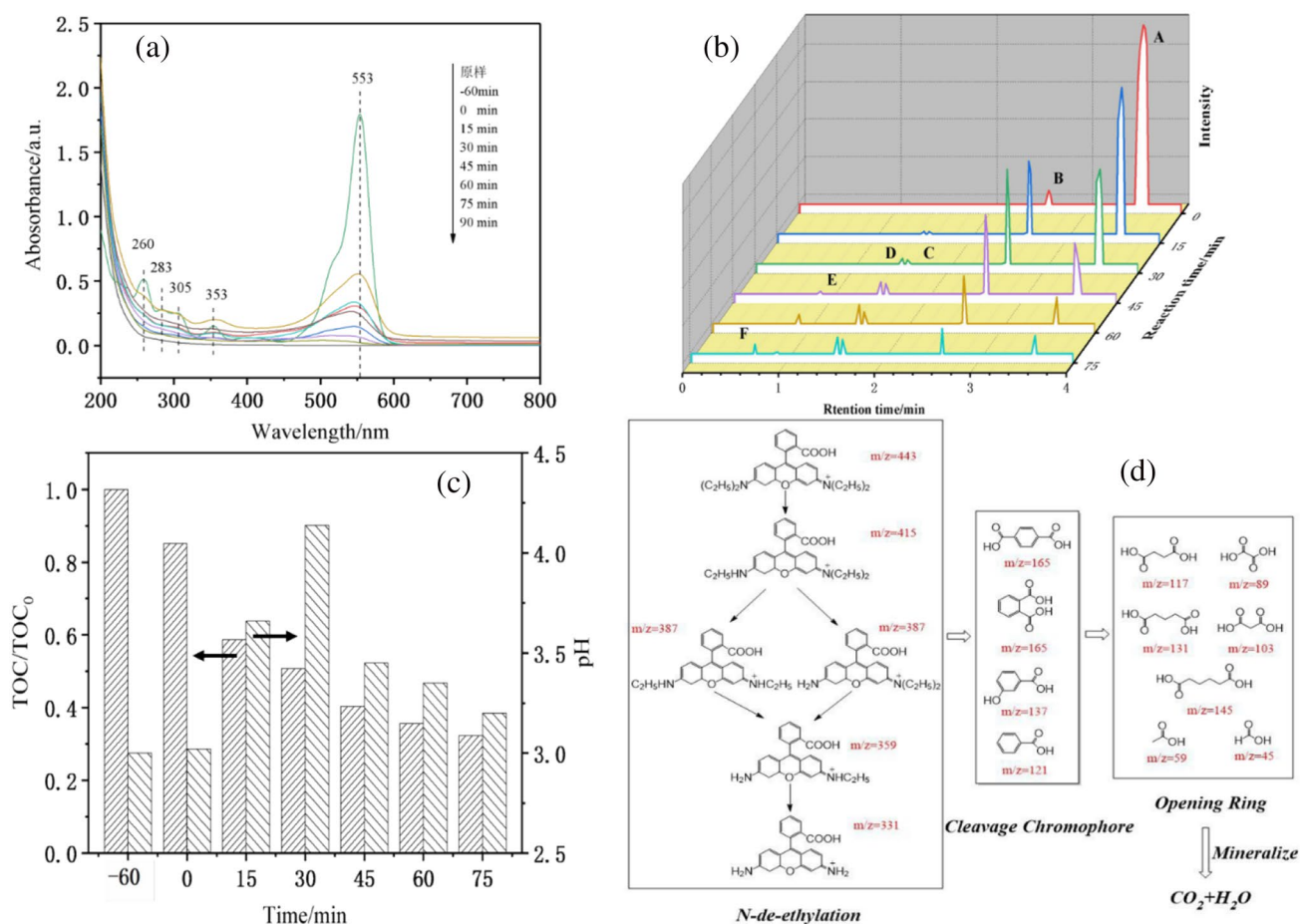


**Fig. 5** Degradation process of RhB in Vis/Fe-g-C<sub>3</sub>N<sub>4</sub>/PMS system: **a** UV-Vis spectra of products; **b** HPLC chromatogram; **c** changes of TOC and pH and **d** proposed degradation path

of the RhB degradation process was determined and shown in Fig. 5c. TOC removal increased and reached 67.67% at 75 min, which means that the mineralized decomposition of RhB happened. The pH of the solution increased first and then decreased. The former was due to the decomposition of RhB, and the latter was due to the generation of acid intermediates such as benzoic acid, adipic acid, and glutaric acid, consistent with the result of HPLC-MS. Therefore, the path of catalytic degradation for RhB in Vis/Fe-g-C<sub>3</sub>N<sub>4</sub>/PMS was inferred and shown in Fig. 5d. The decomposition path of RhB mainly included four stages, including deethylation, color group cracking, open-ring small molecule generation, and mineralized to CO<sub>2</sub> and H<sub>2</sub>O.

### Synergic Mechanism

R-hydroxyethanol (EtOH) and tert-butanol without R-Hydroxy (TBA) as a quencher of free radicals were used to determine the existence forms of sulfate and hydroxyl radical in solution [35]. EtOH simultaneously quenched SO<sub>4</sub><sup>•-</sup> and ·OH, and TBA for ·OH. 1,4-benzoquinone (BQ)

was as ·O<sub>2</sub><sup>-</sup> quencher, EDTA-2Na as h<sup>+</sup> quencher, NaN<sub>3</sub> as <sup>1</sup>O<sub>2</sub>, ·OH and SO<sub>4</sub><sup>•-</sup> quencher [52]. Therefore, EDTA-2Na, NaN<sub>3</sub>, EtOH, BQ, and TBA were used to attain the contributed capacity of h<sup>+</sup>, ·O<sub>2</sub><sup>-</sup>, <sup>1</sup>O<sub>2</sub>, ·OH and SO<sub>4</sub><sup>•-</sup>. To guarantee the free radicals quenching completely, all quenchers were 50 times PMS in molar concentration. The effects of different quenchers addition on RhB degradation were shown in Fig. 6a. By calculating the contributed degree (Table S3), the order of active groups was <sup>1</sup>O<sub>2</sub> > SO<sub>4</sub><sup>•-</sup> > h<sup>+</sup> > ·OH > ·O<sub>2</sub><sup>-</sup>. Note that the degradation efficiency of RhB in the system of Vis/Fe-g-C<sub>3</sub>N<sub>4</sub>/PMS with EDTA-2Na was 47.3%, which was attributed to h<sup>+</sup>. However, the contributor degree of h<sup>+</sup> calculated by other quenching experiments was 12.5%, which means the remained h<sup>+</sup> was the intermediate active product for generating <sup>1</sup>O<sub>2</sub> and ·OH (Eqs. (8) and (9)). Therefore, h<sup>+</sup>, SO<sub>4</sub><sup>•-</sup>, and <sup>1</sup>O<sub>2</sub> were the main active species in Vis/Fe-g-C<sub>3</sub>N<sub>4</sub>/PMS system, different from the co-doping g-C<sub>3</sub>N<sub>4</sub> with PMS decomposing RhB [45], which shows that more <sup>1</sup>O<sub>2</sub> participated in the degradation process. Involved possible reaction equations were shown in Eqs. (5–17) [32], and the decomposition



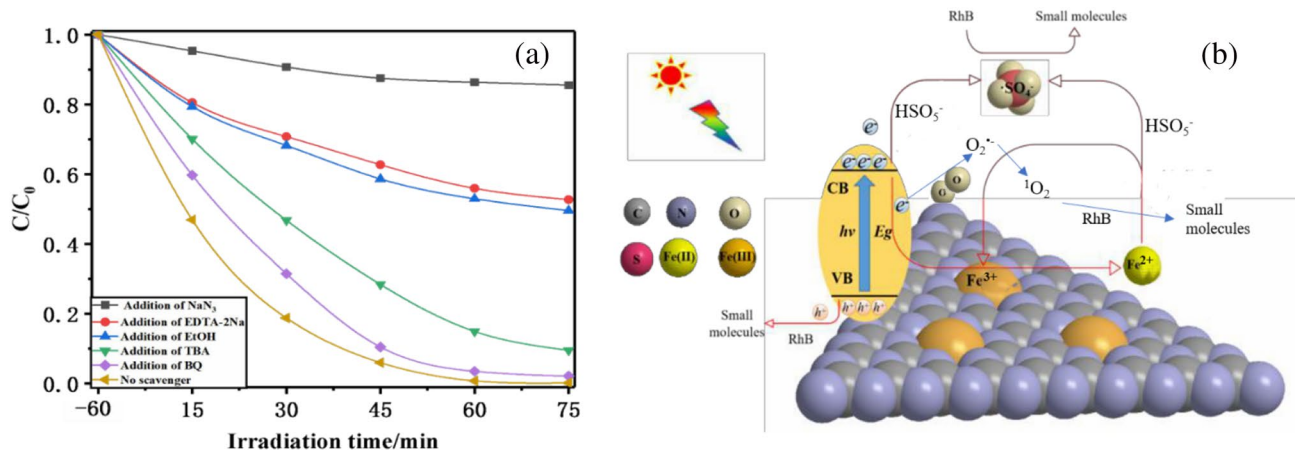


**Fig. 6** Proposed mechanism for photodegradation of RhB on Vis/Fe-g-C<sub>3</sub>N<sub>4</sub>/PMS: **a** free radicals quenching and **b** mechanism scheme

mechanism of RhB in Vis/Fe-g-C<sub>3</sub>N<sub>4</sub>/PMS system was provided in Fig. 6b. Exposure to visible light, electrons of Fe-g-C<sub>3</sub>N<sub>4</sub> was activated to conductive band, and electron-hole was kept in its valence band (Eq. (5)). Electron activated by visible light reacted with PMS to generate sulfate radical ( $E(\text{HSO}_5^-/\text{SO}_4^{\cdot-}) = 1.75 \text{ V}$ ) [39], and O adsorbed on the surface of catalyst was reduced to  $\text{O}_2^{\cdot-}$  ( $E(\text{O}_2/\text{O}_2^{\cdot-}) = -0.16 \text{ V}$ ).  $\text{O}_2^{\cdot-}$  further reacted with  $\text{H}_2\text{O}$  to generate  $^1\text{O}_2$ . The electron-hole can decompose organic molecules due to its strong oxidation [15], meanwhile  $h^+$  can generate strong oxidation activators like  $^1\text{O}_2$  and  $\cdot\text{OH}$  by Eqs. (8 and 9). Coordinated  $\text{Fe}^{3+}$  accepted electron to be reduced to  $\text{Fe}^{2+}$  (Eq. (10)), while  $\text{HSO}_5^-$  oxidized  $\text{Fe}^{2+}$  on the surface of Fe-g-C<sub>3</sub>N<sub>4</sub> into  $\text{Fe}^{3+}$ , and  $\text{Fe}^{3+}$  was reduced  $\text{Fe}^{2+}$  by photocatalysis, then which becomes a cycle and avoids the generation of iron sludge (Eqs. (10–12)) [5]. The free electron and hole generated from g-C<sub>3</sub>N<sub>4</sub> under visible light irradiation can be separated efficiently due to  $\text{HSO}_5^-$  and  $\text{Fe}^{3+}$  consuming electrons. The more  $^1\text{O}_2$  generation maybe by Eq. (6), which indicates that the heterojunction structure of Fe-g-C<sub>3</sub>N<sub>4</sub> decreased the recombination of electrons [29] and holes so that photo-generated electron has more chance to react with adsorbed  $\text{O}_2$  and generated more  $^1\text{O}_2$ . Besides, resulted in massive  $h^+$  can generate strong oxidation activators like  $^1\text{O}_2$  by Eqs. (8, 15 and 16). The more  $^1\text{O}_2$  generation proved this compared with the co-doping g-C<sub>3</sub>N<sub>4</sub> with PMS decomposing RhB [45]. Therefore, photocatalysis (Eq. (5)) and PMS activity process (Eqs. (6 and 7)) demonstrated a synergistic effect, which promotes the generation of  $^1\text{O}_2$ ,  $h^+$  and  $\text{SO}_4^{\cdot-}$ . Besides, sulfate radicals may react with adsorbed water molecules to form hydroxyl radicals (Eq. (14)). Therefore,  $h^+$ ,  $\cdot\text{O}_2^-$ ,  $^1\text{O}_2$ ,  $\cdot\text{OH}$  and  $\text{SO}_4^{\cdot-}$  were the activated species of decomposing RhB, and RhB was ultimately devastated into small molecules and even mineralized into  $\text{CO}_2$  and  $\text{H}_2\text{O}$  (Eq. (17)).

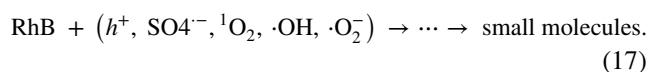
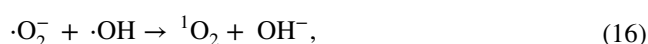
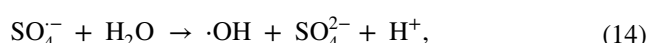
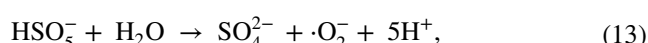
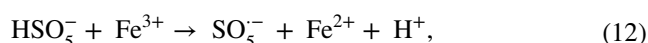
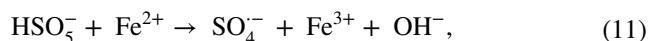
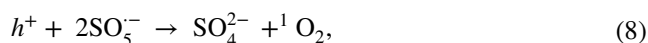
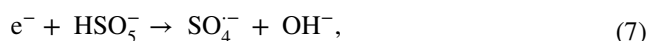
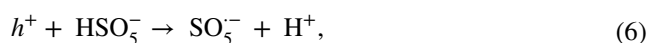
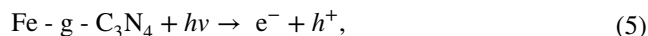
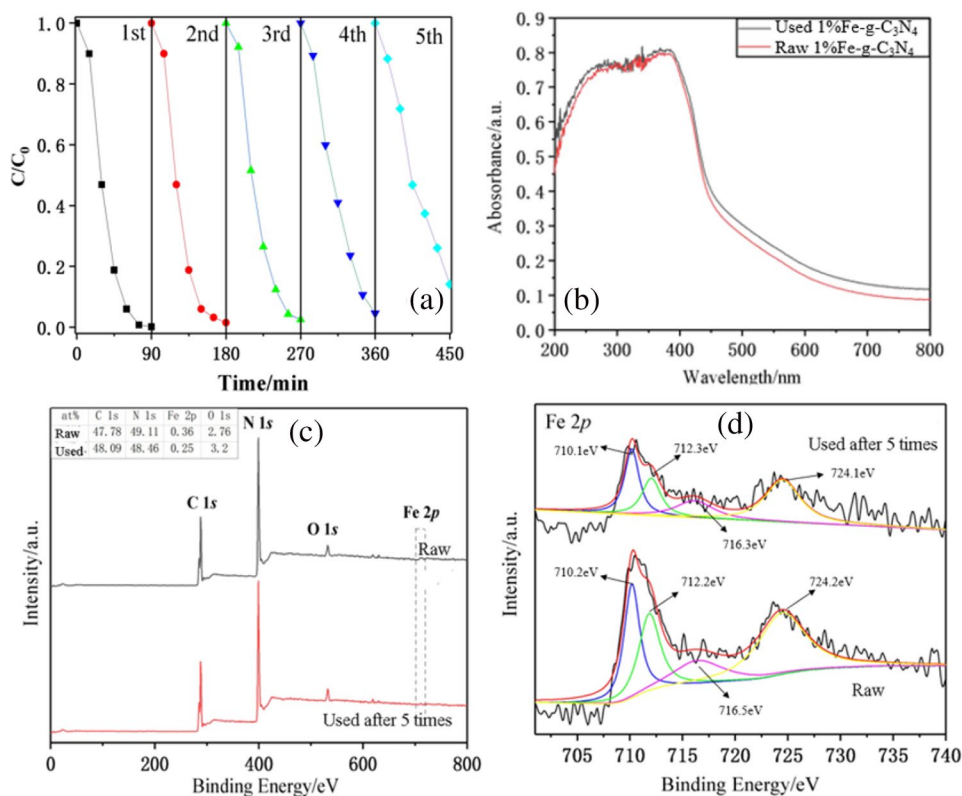


**Fig. 7** Degradation of RhB using the recycled Fe-g-C<sub>3</sub>N<sub>4</sub> (a), and UV-vis spectra (b), XPS wide scanning spectra (c) and XPS spectra of Fe 2p (d) of 1% Fe-g-C<sub>3</sub>N<sub>4</sub> before and after using



## The Stabilization of Catalyst

The recyclable capacity of catalysts is an important parameter, which is shown in Fig. 7a. After five cycle reaction, the decomposition efficiency of RhB by Fe-g-C<sub>3</sub>N<sub>4</sub> decreased gradually, which may be explained by the partial loss of iron on its surface. To further verify this result, original Fe-g-C<sub>3</sub>N<sub>4</sub>, used for 5 times, was determined by XPS, and shown in Fig. 7c, d. Fe content on the surface of used Fe-g-C<sub>3</sub>N<sub>4</sub> decreased from 0.36 to 0.25% (Fig. 7c). Besides, two peaks of 710.2 eV and 712.2 eV for Fe 2p<sub>3/2</sub> were ascribed to Fe<sup>2+</sup> and Fe<sup>3+</sup> respectively [22]. Fe<sup>2+</sup> increased from 53.0 to 55.1%, while Fe<sup>3+</sup> decreased from 47.0 to 44.9%. Therefore, iron loss was the main cause of catalyst reduction and iron was dissolved in the form of iron oxides. Fe-g-C<sub>3</sub>N<sub>4</sub> needs to be modified by this path. XRD, FT-IR, and UV-Vis were further performed to determine the stability of Fe-g-C<sub>3</sub>N<sub>4</sub> catalytic activity, and shown in Fig. S5–6 and Fig. 7b. The structures of Fe-g-C<sub>3</sub>N<sub>4</sub> before and after use had no obvious difference. However, the peak density of Fe-g-C<sub>3</sub>N<sub>4</sub> at 27.5° decreased after use, which can be explained by the iron loss destroying the interlayer stacking structure of Fe-g-C<sub>3</sub>N<sub>4</sub>. The semiconductor performances of Fe-g-C<sub>3</sub>N<sub>4</sub> before and after using were the same, indicating a good stability of photocatalysis activity.

## Conclusion

This work aims to explore the synergistic efficiency of Fe-g-C<sub>3</sub>N<sub>4</sub>, PMS and photocatalysis for decomposing RhB. The obtained Fe-g-C<sub>3</sub>N<sub>4</sub> was characterized by XRD, UV-Vis, DRS, FTIR, BET and XPS, which indicates that Fe of Fe-g-C<sub>3</sub>N<sub>4</sub> existed in the form of Fe–N coordination bond, and had more stronger absorption capacity of visible light due to the decrease of gap between valence and conductive band. A sulfate radical-based advanced oxidation processes combined with Fe-g-C<sub>3</sub>N<sub>4</sub> photocatalysis by visible light irradiation was established for decomposing Rhodamine B. The degradation efficiency of RhB in the system of Vis/Fe-g-C<sub>3</sub>N<sub>4</sub>/PMS reached 99.8%, and the degradation process of Fe-g-C<sub>3</sub>N<sub>4</sub> accorded with a pseudo-first-order kinetic model, which shows a synergistic effect of SR-AOPs and photocatalysis. The radical quenching experiment has fully proved that  $h^+$ ,  $SO_4^{\cdot-}$  and  $^1O_2$  were the main active species during RhB degradation, and the order of radical contributed degree was  $^1O_2 > SO_4^{\cdot-} > h^+ > \cdot OH > \cdot O_2^-$ . The more  $^1O_2$  generation maybe due to the heterojunction structure of Fe-g-C<sub>3</sub>N<sub>4</sub> for less recombination of electron–hole pairs. The semiconductor performances of Fe-g-C<sub>3</sub>N<sub>4</sub> had good stability of photocatalysis activity. The degradation mechanism of RhB in the system of Vis/Fe-g-C<sub>3</sub>N<sub>4</sub>/PMS was proposed.

**Supplementary Information** The online version contains supplementary material available at <https://doi.org/10.1007/s11814-024-00066-9>.

**Acknowledgements** This work was supported by the National Natural Science Foundation of China (U20A20325).

**Author Contributions** XZ: experiment design and manuscript writing; ZS: preparation and characterization of catalyst, and manuscript writing; ZY: data analysis and discussion, manuscript writing revision; FH: catalyst and AOPs experiment; SW: preparation and characterization of catalyst; WL: preparation and characterization of catalyst; JW: experiment design, data analysis and manuscript revision.

**Data availability** Data in this manuscript has been provided in the supplementary material.

## Declarations

**of Interest** The authors declare no competing interests.

**Ethics approval** Not applicable.

**Consent to participate and publish** The Hefei University of Technology and Anhui Maanshan Iron and Steel Mining Resources Group are aware of this submission and every co-author approved this submission.

## References

- P. Akhter, A. Arshad, A. Saleem, M. Hussain, Recent development in non-metal-doped titanium dioxide photocatalysts for different dyes degradation and the study of their strategic factors: a review. *Catalysts* **12**, 1331 (2022). <https://doi.org/10.3390/catal12111331>
- M. Asif, M. Zafar, P. Akhter, M. Hussain, A. Umer, A. Razzaq, W.Y. Kim, Effect of urea addition on anatase phase enrichment and nitrogen doping of TiO<sub>2</sub> for photocatalytic abatement of methylene blue. *Appl. Sci.* **11**, 8264 (2021). <https://doi.org/10.3390/app11178264>
- K. Azam, R. Raza, N. Shezad, M. Shabir, W. Yang, N. Ahmad, I. Shafiq, P. Akhter, A. Razzaq, M. Hussain, Development of recoverable magnetic mesoporous carbon adsorbent for removal of methyl blue and methyl orange from wastewater. *J. Environ. Chem. Eng.* **8**, 104220 (2020). <https://doi.org/10.1016/j.jece.2020.104220>
- K. Azam, N. Shezad, I. Shafiq, P. Akhter, F. Akhtar, F. Jamil, S. Shafique, Y.K. Park, M. Hussain, A review on activated carbon modifications for the treatment of wastewater containing anionic dyes. *Chemosphere* **306**, 135566 (2022). <https://doi.org/10.1016/j.chemosphere.2022.135566>
- A.A. Babaei, M. Golshan, B. Kakavandi, A heterogeneous photocatalytic sulfate radical-based oxidation process for efficient degradation of 4-chlorophenol using TiO anchored on Fe oxides@ carbon. *Process. Saf. Environ.* **149**, 35–47 (2021). <https://doi.org/10.1016/j.psep.2020.10.028>
- P. Bhavani, D.P. Kumar, M. Hussain, K. Jeon, Y.K. Park, Recent advances in wide solar spectrum active W<sub>18</sub>O<sub>49</sub>-based photocatalysts for energy and environmental applications. *Catal. Rev.* (2021). <https://doi.org/10.1080/01614940.2022.2038472>
- D.D. Chen, J.G. Liu, Z.Z. Jia, J.Z. Fang, F. Yang, Y.M. Tang, K. Wu, Z. Liu, Z.Q. Fang, Efficient visible-light-driven hydrogen evolution and Cr(VI) reduction over porous P and Mo co-doped g-C<sub>3</sub>N<sub>4</sub> with feeble N vacancies photocatalyst. *J. Hazard. Mater.* **361**, 294–304 (2019). <https://doi.org/10.1016/j.jhazmat.2018.09.006>
- K. Chen, Z.G. Chai, C. Li, L.R. Shi, M.X. Liu, Q. Xie, Y.F. Zhang, D.S. Xu, A. Manivannan, Z.F. Liu, Catalyst-free growth of three-dimensional graphene flakes and graphene/g-C<sub>3</sub>N<sub>4</sub> composite for hydrocarbon oxidation. *ACS Nano* **10**(3), 3665–3673 (2016). <https://doi.org/10.1021/acs.nano.6b00113>
- H. Cui, S.Y. Dong, K.K. Wang, M.S. Luan, T.L. Huang, Synthesis of a novel Type-II In<sub>2</sub>S<sub>3</sub>/Bi<sub>2</sub>MoO<sub>6</sub> heterojunction photocatalyst: excellent photocatalytic performance and degradation mechanism for Rhodamine B. *Sep. Purif. Technol.* (2021). <https://doi.org/10.1016/j.seppur.2020.117758>
- Y.J. Cui, J.S. Zhang, G.G. Zhang, J.H. Huang, P. Liu, M. Antonietti, X.C. Wang, Synthesis of bulk and nanoporous carbon nitride polymers from ammonium thiocyanate for photocatalytic hydrogen evolution. *J. Mater. Chem.* **21**(34), 13032–13039 (2011). <https://doi.org/10.1039/c1jm11961c>
- Y. Ding, K.P. Cui, X.Y. Liu, C.X. Li, Z. Guo, M.S. Cui, Y.H. Chen, Axial g-C<sub>3</sub>N<sub>4</sub> coordinated iron(III) phthalocyanine mediated ultra-efficient peroxymonosulfate activation for high-valent iron species generation. *Appl. Catal. A-Gen.* **641**, 118679 (2022). <https://doi.org/10.1016/j.apcata.2022.118679>
- M. El Alouani, S. Alehyen, H. El Hadki, H. Saufi, A. Elhalil, O.K. Kabbaj, M.H. Taibi, Synergetic influence between adsorption and photodegradation of Rhodamine B using synthesized fly ash based inorganic polymer. *Surf. Interfaces* **24**, 101136 (2021). <https://doi.org/10.1016/j.surfin.2021.101136>
- S. Fang, Y. Xia, K.L. Lv, Q. Li, J. Sun, M. Li, Effect of carbon-dots modification on the structure and photocatalytic activity of g-C<sub>3</sub>N<sub>4</sub>. *Appl. Catal. B-Environ.* **185**, 225–232 (2016). <https://doi.org/10.1016/j.apcatb.2015.12.025>
- J.T. Gao, Y. Wang, S.J. Zhou, W. Lin, Y. Kong, A facile one-step synthesis of Fe-doped g-C<sub>3</sub>N<sub>4</sub> nanosheets and their improved visible-light photocatalytic performance. *ChemCatChem* **9**(9), 1708–1715 (2017). <https://doi.org/10.1002/cctc.201700492>
- Y. Gong, X. Zhao, H. Zhang, B. Yang, K. Xiao, T. Guo, J.J. Zhang, H.X. Shao, Y.B. Wang, G. Yu, MOF-derived nitrogen doped carbon modified g-C<sub>3</sub>N<sub>4</sub> heterostructure composite with enhanced photocatalytic activity for bisphenol A degradation with peroxymonosulfate under visible light irradiation. *Appl. Catal. B-Environ.* **233**, 35–45 (2018). <https://doi.org/10.1016/j.apcatb.2018.03.077>
- M. Hasanpour, M. Hatami, Photocatalytic performance of aerogels for organic dyes removal from wastewaters: review study. *J. Mol. Liq.* **309**, 113094 (2020). <https://doi.org/10.1016/j.molliq.2020.113094>
- S.Z. Hu, R.R. Jin, G. Lu, D. Liu, J.Z. Gui, The properties and photocatalytic performance comparison of Fe<sup>3+</sup>-doped g-C<sub>3</sub>N<sub>4</sub> and Fe<sub>2</sub>O<sub>3</sub>/g-C<sub>3</sub>N<sub>4</sub> composite catalysts. *Rsc Adv.* **4**(47), 24863–24869 (2014). <https://doi.org/10.1039/c4ra03290j>
- J. Ji, Y. Liu, X.Y. Yang, J. Xu, X.Y. Li, Multiple response optimization for high efficiency energy saving treatment of rhodamine B wastewater in a three-dimensional electrochemical reactor. *J. Environ. Manage.* **218**, 300–308 (2018). <https://doi.org/10.1016/j.jenvman.2018.04.071>
- X. Jing, J. Yuan, D. Cai, B. Li, D. Hu, J. Li, Concentrating and recycling of high-concentration printing and dyeing wastewater by a disc tube reverse osmosis-Fenton oxidation/low temperature crystallization process. *Sep. Purif. Technol.* **266**, 118583 (2021). <https://doi.org/10.1016/j.seppur.2021.118583>
- G.J. Joshiba, P.S. Kumar, M. Govarthan, P.T. Ngeagni, A. Abilarasu, C.F. Carolin, Investigation of magnetic silica nanocomposite immobilized *Pseudomonas fluorescens* as a biosorbent for the effective sequestration of Rhodamine B from aqueous systems. *Environ. Pollut.* **269**, 116173 (2021). <https://doi.org/10.1016/j.envpol.2020.116173>

21. X.J. Lang, X.D. Chen, J.C. Zhao, Heterogeneous visible light photocatalysis for selective organic transformations. *Chem. Soc. Rev.* **43**(1), 473–486 (2014). <https://doi.org/10.1039/C3CS60188A>
22. Q. Li, H. Xu, G. Zhou, F. Cheng, M. Wang, J. Zhang, Y. Wang, X. Huang, Q. Wang, Sulfite activation by Fe-doped g-C<sub>3</sub>N<sub>4</sub> for metronidazole degradation. *Sep. Purif. Technol.* **272**, 118928 (2021). <https://doi.org/10.1016/j.seppur.2021.118928>
23. Z. Li, Q. Chen, Q. Lin, Y. Chen, X. Liao, H. Yu, C. Yu, Three-dimensional P-doped porous g-C<sub>3</sub>N<sub>4</sub> nanosheets as an efficient metal-free photocatalyst for visible-light photocatalytic degradation of Rhodamine B model pollutant. *J. Taiwan Inst. Chem. E* **114**, 249–262 (2020). <https://doi.org/10.1016/j.jtice.2020.09.019>
24. A.Y. Liu, M.L. Cohen, Prediction of new low compressibility solids. *Science* **245**(4920), 841–842 (1989). <https://doi.org/10.1126/science.245.4920.841>
25. C. Liu, L. Liu, X. Tian, Y. Wang, R. Li, Y. Zhang, Z. Song, B. Xu, W. Chu, F. Qi, A. Ikhlaq, Coupling metal–organic frameworks and g-C<sub>3</sub>N<sub>4</sub> to derive Fe@N-doped graphene-like carbon for peroxymonosulfate activation: Upgrading framework stability and performance. *Appl. Catal. B-Environ.* **255**, 117763 (2019). <https://doi.org/10.1016/j.apcatb.2019.117763>
26. L. Liu, Z. Chen, J. Zhang, D. Shan, Y. Wu, L. Bai, B. Wang, Treatment of industrial dye wastewater and pharmaceutical residue wastewater by advanced oxidation processes and its combination with nanocatalysts: a review. *J. Water Process. Eng.* **42**, 102122 (2021). <https://doi.org/10.1016/j.jwpe.2021.102122>
27. C. Lops, A. Ancona, K. Di Cesare, B. Dumontel, N. Garino, G. Canavese, S. Hernandez, V. Cauda, Sonophotocatalytic degradation mechanisms of Rhodamine B dye via radicals generation by micro- and nano-particles of ZnO. *Appl. Catal. B-Environ.* **243**, 629–640 (2019). <https://doi.org/10.1016/j.apcatb.2018.10.078>
28. Y.S. Lu, Z. Wang, Y.F. Xu, Q. Liu, G.R. Qian, Fe<sub>2</sub>(MoO<sub>4</sub>)<sub>3</sub> as a novel heterogeneous catalyst to activate persulfate for Rhodamine B degradation. *Desalin. Water Treat.* **57**(17), 7898–7909 (2016). <https://doi.org/10.1080/19443994.2015.1033476>
29. I. Mahboob, I. Shafiq, S. Shafique, P. Akhter, M. Munir, M. Saeed, M.S. Nazir, U. Amjad, F. Jamil, N. Ahmad, Y.K. Park, M. Hussain, Porous Ag<sub>3</sub>VO<sub>4</sub>/KIT-6 composite: synthesis, characterization and enhanced photocatalytic performance for degradation of Congo Red. *Chemosphere* **311**, 137180 (2023). <https://doi.org/10.1016/j.chemosphere.2022.137180>
30. Q.G. Meng, M.Z. Yuan, H.Q. Lv, Z. Chen, G.F. Zhou, Z.H. Chen, X. Wang, Facile construction of metal-free g-C<sub>3</sub>N<sub>4</sub> isotype heterojunction with highly enhanced visible-light photocatalytic performance. *Chem. Sel.* **2**(24), 6970–6978 (2017). <https://doi.org/10.1002/slct.201700705>
31. W. Meng, Y. Wang, Y. Zhang, C. Liu, Z. Wang, Z. Song, B. Xu, F. Qi, A. Ikhlaq, Degradation Rhodamine B dye wastewater by sulfate radical-based visible light-fenton mediated by LaFeO<sub>3</sub>: reaction mechanism and empirical modeling. *J. Taiwan Inst. Chem. E* **111**, 162–169 (2020). <https://doi.org/10.1016/j.jtice.2020.04.005>
32. S. Meng, Z. Nan, Selective degradation in Fenton-like reaction catalyzed by Na and Fe Co-doped g-C<sub>3</sub>N<sub>4</sub> catalyst. *Sep. Purif. Technol.* **309**, 123026 (2023). <https://doi.org/10.1016/j.seppur.2022.123026>
33. P.V. Nidheesh, R. Gandhimathi, S.T. Ramesh, Degradation of dyes from aqueous solution by Fenton processes: a review. *Environ. Sci. Pollut. R* **20**(4), 2099–2132 (2013). <https://doi.org/10.1007/s11356-012-1385-z>
34. W.J. Ong, L.L. Tan, Y.H. Ng, S.T. Yong, S.P. Chai, Graphitic carbon nitride (g-C<sub>3</sub>N<sub>4</sub>)-based photocatalysts for artificial photosynthesis and environmental remediation: are we a step closer to achieving sustainability? *Chem. Rev.* **116**(12), 7159–7329 (2016). <https://doi.org/10.1021/acs.chemrev.6b00075>
35. Y.W. Pan, M.H. Zhou, Y. Zhang, J.J. Cai, B. Li, X.J. Sheng, Enhanced degradation of Rhodamine B by pre-magnetized Fe<sup>0</sup>/PS process: parameters optimization, mechanism and interferences of ions. *Sep. Purif. Technol.* **203**, 66–74 (2018). <https://doi.org/10.1016/j.seppur.2018.03.039>
36. R. Rashid, I. Shafiq, P. Akhter, M.J. Iqbal, M. Hussain, A state-of-the-art review on wastewater treatment techniques: the effectiveness of adsorption method. *Environ. Sci. Pollut. R* **28**, 9050–9066 (2021). <https://doi.org/10.1007/s11356-021-12395-x>
37. R. Rashid, I. Shafiq, M.J. Iqbal, M. Shabir, P. Akhter, M.H. Hamayun, A. Ahmed, M. Hussain, Synergistic effect of NS co-doped TiO<sub>2</sub> adsorbent for removal of cationic dyes. *J. Environ. Chem. Eng.* **9**, 105480 (2021). <https://doi.org/10.1016/j.jece.2021.105480>
38. M. Shabir, M. Yasin, M. Hussain, I. Shafiq, P. Akhter, A.S. Nizami, B.H. Jeon, Y.K. Park, A review on recent advances in the treatment of dye-polluted wastewater. *J. Ind. Eng. Chem.* **112**, 1–19 (2022). <https://doi.org/10.1016/j.jiec.2022.05.013>
39. H.X. Shao, X. Zhao, Y.B. Wang, R. Mao, Y. Wang, M. Qiao, S. Zhao, Y.F. Zhu, Synergetic activation of peroxymonosulfate by Co<sub>3</sub>O<sub>4</sub> modified g-C<sub>3</sub>N<sub>4</sub> for enhanced degradation of diclofenac sodium under visible light irradiation. *Appl. Catal. B-Environ.* **218**, 810–818 (2017). <https://doi.org/10.1016/j.apcatb.2017.07.016>
40. I. Shafiq, M. Hussain, N. Shehzad, I.M. Maafa, P. Akhter, U. Amjad, S. Shafique, A. Razzaq, W. Yang, M. Tahir, N. Russo, The effect of crystal facets and induced porosity on the performance of monoclinic BiVO<sub>4</sub> for the enhanced visible-light driven photocatalytic abatement of methylene blue. *J. Environ. Chem. Eng.* **7**, 103265 (2019). <https://doi.org/10.1016/j.jece.2019.103265>
41. N. Shehzad, M. Zafar, M. Ashfaq, A. Razzaq, P. Akhter, N. Ahmad, A. Hafeez, K. Azam, M. Hussain, W.Y. Kim, Development of AgFeO<sub>2</sub>/rGO/TiO<sub>2</sub> ternary composite photocatalysts for enhanced photocatalytic dye decolorization. *Crystals* **10**, 923 (2020). <https://doi.org/10.3390/cryst10100923>
42. Z. Siraj, I.M. Maafa, I. Shafiq, N. Shehzad, P. Akhter, W. Yang, M. Hussain, KIT-6 induced mesostructured TiO<sub>2</sub> for photocatalytic degradation of methyl blue. *Environ. Sci. Pollut. R* **28**, 53340–53352 (2021). <https://doi.org/10.1007/s11356-021-14442-z>
43. L.M. Skjolding, L.V. Jorgensen, K.S. Dyhr, C.J. Koppl, U.S. McKnight, P. Bauer-Gottwein, P. Mayer, P.L. Bjerg, A. Baun, Assessing the aquatic toxicity and environmental safety of tracer compounds Rhodamine B and Rhodamine WT. *Water Res.* **197**, 117109 (2021). <https://doi.org/10.1016/j.watres.2021.117109>
44. B.J. Sun, W.J. Ma, N. Wang, P. Xu, L.J. Zhang, B.N. Wang, H.H. Zhao, K.Y.A. Lin, Y.C. Du, Polyaniline: a new metal-free catalyst for peroxymonosulfate activation with highly efficient and durable removal of organic pollutants (vol 53, pg 9771, 2021) (Retraction of Vol 53, Pg 3451, 2021). *Environ. Sci. Technol.* **55**(5), 3451–3451 (2021). <https://doi.org/10.1021/acs.est.0c07981>
45. L.L. Wang, X. Guo, Y.Y. Chen, S.S. Ai, H.M. Ding, Cobalt-doped g-C<sub>3</sub>N<sub>4</sub> as a heterogeneous catalyst for photo-assisted activation of peroxymonosulfate for the degradation of organic contaminants. *Appl. Surf. Sci.* **467**, 954–962 (2019). <https://doi.org/10.1016/j.apsusc.2018.10.262>
46. M.Q. Wang, W.H. Yang, H.H. Wang, C. Chen, Z.Y. Zhou, S.G. Sun, Pyrolyzed Fe-N-C composite as an efficient non-precious metal catalyst for oxygen reduction reaction in acidic medium. *Acs Catal.* **4**(11), 3928–3936 (2014). <https://doi.org/10.1021/cs500673k>
47. R.A. Wang, X.Y. Zhang, L.L. Zhao, J. Feng, T. Wei, Y.M. Ren, Y.Q. Shen, In-situ synthesis of Fe and O co-doped g-C<sub>3</sub>N<sub>4</sub> to enhance peroxymonosulfate activation with favorable charge transfer for efficient contaminant decomposition. *J. Taiwan Inst. Chem. E* **115**, 198–207 (2020). <https://doi.org/10.1016/j.jtice.2020.10.022>

48. X. Wang, M. He, Z. Nan, Effects of adsorption capacity and activity site on Fenton-like catalytic performance for Na and Fe co-doped g-C<sub>3</sub>N<sub>4</sub>. *Sep. Purif. Technol.* **256**, 117765 (2021). <https://doi.org/10.1016/j.seppur.2020.117765>
49. Y. Wang, C. Liu, Y. Zhang, W. Meng, B. Yu, S. Pu, D. Yuan, F. Qi, B. Xu, W. Chu, Sulfate radical-based photo-Fenton reaction derived by CuBi<sub>2</sub>O<sub>4</sub> and its composites with α-Bi<sub>2</sub>O<sub>3</sub> under visible light irradiation: catalyst fabrication, performance and reaction mechanism. *Appl. Catal. B-Environ.* **235**, 264–273 (2018). <https://doi.org/10.1016/j.apcatb.2018.04.058>
50. M.N. Van, O.L.T. Mai, C.P. Do, H.L. Thi, C.P. Manh, H.N. Manh, D.P. Thi, B.D. Danh, Fe-Doped g-C<sub>3</sub>N<sub>4</sub>: high-performance photocatalysts in rhodamine B decomposition. *Polymers* **12**, 1963 (2020). <https://doi.org/10.3390/polym12091963>
51. W. Xiao, X. Jiang, X. Liu, W. Zhou, Z.N. Garba, I. Lawan, L. Wang, Z. Yuan, Adsorption of organic dyes from wastewater by metal-doped porous carbon materials. *J. Clean. Prod.* **284**, 124773 (2021). <https://doi.org/10.1016/j.jclepro.2020.124773>
52. J. Xie, Y.L. Cao, D.Z. Jia, Y.Z. Li, Dahlia-shaped BiOCl<sub>x</sub>I<sub>1-x</sub> structures prepared by a facile solid-state method: Evidence and mechanism of improved photocatalytic degradation of rhodamine B dye. *J. Colloid Interf. Sci.* **503**, 115–123 (2017). <https://doi.org/10.1016/j.jcis.2017.05.016>
53. H. Xu, B. Yang, Y. Liu, F. Li, X. Song, X. Cao, W. Sand, Evolution of microbial populations and impacts of microbial activity in the anaerobic-oxic-settling-anaerobic process for simultaneous sludge reduction and dyeing wastewater treatment. *J. Clean. Prod.* **282**, 124403 (2021). <https://doi.org/10.1016/j.jclepro.2020.124403>
54. S. Yang, Y. Feng, N. Liu, Y. Zhao, X. Wang, Z. Zhang, H. Chen, Y. Yu, Enhancement on the removal of Rhodamine B (RhB) by means of the Enlarged Anode Electric Biological (EAEB) reactor. *Chemosphere* **245**, 125566 (2020). <https://doi.org/10.1016/j.chemosphere.2019.125566>
55. X. Yuan, S. Qu, X. Huang, X. Xue, C. Yuan, S. Wang, L. Wei, P. Cai, Design of core-shelled g-C<sub>3</sub>N<sub>4</sub>@ZIF-8 photocatalyst with enhanced tetracycline adsorption for boosting photocatalytic degradation. *Chem. Eng. J.* **416**, 129148 (2021). <https://doi.org/10.1016/j.cej.2021.129148>
56. G.G. Zhang, S.H. Zang, X.C. Wang, Layered Co(OH)<sub>2</sub> deposited polymeric carbon nitrides for photocatalytic water oxidation. *Acs Catal.* **5**(2), 941–947 (2015). <https://doi.org/10.1021/cs502002u>

**Publisher's Note** Springer Nature remains neutral with regard to jurisdictional claims in published maps and institutional affiliations.

Springer Nature or its licensor (e.g. a society or other partner) holds exclusive rights to this article under a publishing agreement with the author(s) or other rightsholder(s); author self-archiving of the accepted manuscript version of this article is solely governed by the terms of such publishing agreement and applicable law.